

From nonreciprocal to charge-4e supercurrents in Ge-based Josephson devices with tunable harmonic content

Axel Leblanc,^{1,*} Chotivut Tangchingchai,¹ Zahra Sadre Momtaz,² Elyjah Kiyooka,¹ Jean-Michel Hartmann,³ Gonzalo Troncoso Fernandez-Bada,¹ Boris Brun-Barriere,¹ Vivien Schmitt,¹ Simon Zihlmann,¹ Romain Maurand,¹ Étienne Dumur,¹ Silvano De Franceschi,¹ and François Lefloch^{1,†}

¹*Univ. Grenoble Alpes, CEA, Grenoble INP, IRIG, PHELIQS, 38000 Grenoble, France*

²*Institut Néel, CNRS/UGA, Grenoble 38042, France*

³*Univ. Grenoble Alpes, CEA, LETI, 38000 Grenoble, France*

(Dated: November 28, 2023)

Hybrid superconductor(S)-semiconductor(Sm) devices bring a range of new functionalities into superconducting circuits. In particular, hybrid parity-protected qubits and Josephson diodes were recently proposed and experimentally demonstrated. Such devices leverage the non-sinusoidal character of the Josephson current-phase relation (CPR) in highly transparent S-Sm-S junctions. Here we report an experimental study of superconducting quantum-interference devices (SQUIDs) embedding Josephson field-effect transistors fabricated from a SiGe/Ge/SiGe heterostructure grown on a 200-mm silicon wafer. The single-junction CPR shows up to three harmonics with gate tunable amplitude. In the presence of microwave irradiation, the ratio of the first two dominant harmonics, corresponding to single and double Cooper-pair transport processes, is consistently reflected in relative weight of integer and half-integer Shapiro steps. A combination of magnetic-flux and gate-voltage control enables tuning the SQUID functionality from a nonreciprocal Josephson-diode regime with 27 % asymmetry to a π -periodic Josephson regime suitable for the implementation of parity-protected superconducting qubits. These results illustrate the potential of Ge-based hybrid devices as versatile and scalable building blocks of novel superconducting quantum circuits.

I. INTRODUCTION

The recent years have seen a revival of interest toward superconductor(S)-semiconductor(Sm) devices. These hybrid systems leverage, on the one hand, the macroscopic quantum coherence coming from superconductivity and, on the other hand, the field-effect charge control enabled by semiconductor materials. A typical example is the Josephson field-effect transistor (JoFET), a three-terminal device consisting of two superconducting contacts connected by a gate-tunable semiconducting channel. Owing to the superconducting proximity effect, a dissipationless supercurrent can flow through the normal-type semiconductor channel, with a maximal value, the so-called critical current, that depends on the applied gate voltage. A variety of JoFETs have been realized using different semiconductor materials. Some of these JoFETs were used to realize gate-tunable superconducting qubits often called gatemons [1–5] and parametric amplifiers [6–13].

In a JoFET, high-transparency S-Sm contacts enable the phase coherent transfer of m Cooper pairs at a time, resulting in the emergence of $\sin(m\varphi)$ components in the current phase relation (CPR) where φ is the phase difference between the two superconductors [14]. The gate permits to fine tune the critical current amplitude as well as the CPR harmonic composition [15].

In the context of superconducting qubits, the ability to tailor the CPR provides a means to engineer the

support of the wavefunctions encoding the qubit. This idea has led to parity-protected qubits leveraging supercurrents carried by correlated pairs of Cooper pairs in $\sin(2\varphi)$ Josephson elements [16–19]. Along the same line, $\sin(2\varphi)$ Josephson elements for parity protection were recently obtained using S-Sm-S junctions with either an InAs [20, 21] or, as in this work, a Ge channel [22]

Here we investigate the CPR of a Ge-based Josephson junction using an asymmetric SQUID featuring a wide and a narrow JoFET [23]. The CPR Fourier transform exhibits gate-tunable higher harmonics, revealing charge-2e, charge-4e and charge-6e dissipationless transport. Notably, we observe the possibility of suppressing the higher harmonics by polarizing the JoFET near pinch-off. Subsequently, by investigating the response to microwave excitation, we observe half-integer Shapiro steps corroborating the existence of charge-4e supercurrents.

It was recently proposed [24] that non-sinusoidal CPR in nearly symmetric SQUIDs can lead to asymmetric transport characteristics. This behavior, commonly known as superconducting diode effect (SDE), requires time-reversal symmetry broken by a magnetic flux and is highly tunable unlike previously reported realizations based on inversion symmetry breaking [25–31], spin orbit interaction coupled to a Zeeman field [32–35] or magnetic JJ [36]. The diode efficiency vanishes when the SQUID operates in a perfectly symmetric regime, i.e. when the two junctions have the same CPR, or when the SQUID is flux-biased at half the flux quantum. By harnessing the SDE within a SQUID made of two similar JoFETs (we observe diode efficiency up to 27%), we identify its regime of critical current balance. In this configuration, Shapiro steps measurements at half flux quantum bias

* E-mail: axel.leblanc@cea.fr

† E-mail: francois.lefloch@cea.fr

evidences a pronounced reduction in the odd harmonics due to destructive interference within the SQUID.

This realization yields a device primarily governed by a charge-4e supercurrent, effectively creating a $\sin(2\varphi)$ Josephson element, thus opening the pathway for the development of Ge based parity-protected qubits.

II. DEVICE AND MATERIAL PROPERTIES

The initial heterostructure consists of a $\text{Si}_{0.21}\text{Ge}_{0.79}$ virtual substrate (with a 10%Ge/ μm grading from a few % up to 79% of Ge and a 2.5 μm thick $\text{Si}_{0.21}\text{Ge}_{0.79}$ layer on top) grown on a Si(001) wafer. A 16 nm thick Ge quantum well is grown on top of the polished virtual substrate and covered by a 22 nm thick $\text{Si}_{0.21}\text{Ge}_{0.79}$ layer and a 2 nm thick Si cap layer. In accumulation regime the hole mobility μ_h measured in $60 \times 600 \mu\text{m}^2$ Hall bars, reaches $1 \times 10^5 \text{ cm}^2 \text{ V}^{-1} \text{ s}^{-1}$ while the elastic mean free path is estimated to $l_e \approx 1.5 \mu\text{m}$ [37].

The fabrication of the Ge JoFETs starts with the etching of a long mesa (typically 5 μm) with various widths ranging from 1 μm to 10 μm . In a second step, the superconducting contacts are defined by locally etching the Si cap layer and the SiGe top layer, followed by the ex-situ deposition and lift-off of a 50 nm thick Al layer in contact with the Ge quantum well. The aluminium contact has a typical critical temperature of 1.54 K. An AlO_x oxide is then deposited everywhere using Atomic Layer Deposition (ALD). To finish the process, a Ti/Au top gate covers the Ge central channel and slightly overlaps the Al contacts (Fig1. a).

The asymmetric SQUID consists of two Al-Ge-Al JoFETs placed in an Al loop (Fig. 1b). The narrow junction J_n has a width of 1 μm , while the wide junction J_w is 8 μm wide. Both junctions are 300 nm long. In the following experiments, the devices are cooled down to a base temperature of 35 mK. To measure the electrical behavior of J_n (resp. J_w) independently, we apply a large gate voltage on J_w (resp. J_n) (typically 4 V) to suppress the conductance on the respective arm of the SQUID. Both junctions can be fully proximitized and show a non-dissipative current up to a certain switching current (identified as the critical current) that is gate tunable. At full accumulation ($V_G = -2 \text{ V}$), the critical currents are $I_C^n = 158 \text{ nA}$ and $I_C^w = 2.39 \mu\text{A}$ with very remarkable similar gate dependency (Fig. 1c). The $I_C R_N$ product of both junctions are of the order of 100 μeV and very close to the state-of-the art [38–42].

The symmetric SQUID device used to study the SDE is composed of two nearly identical junctions with $W=4 \mu\text{m}$ and $L=300 \text{ nm}$ and shows similar tunable critical current at low temperature.

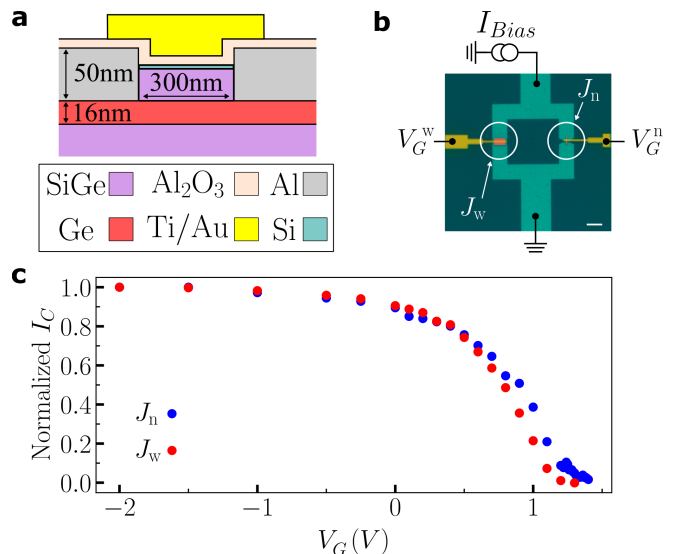


FIG. 1. **Ge/Al Josephson field effect transistors (JoFET) placed in a SQUID.** **a**, Cross-section sketch of a JoFET where the Ge quantum well is contacted by two superconducting aluminium leads. The Ti/Au top gate allows to modify the hole carrier density in the channel. **b**, False color SEM image of the SQUID with a wide (left) and a narrow (right) junctions placed in an aluminium loop (green). Electrostatic gates are shown in yellow. The scale bar is 10 μm . **c**, Critical current of the two junctions normalised to their values at $V_G = -2 \text{ V}$.

III. CURRENT-PHASE RELATION OF A SINGLE Ge/Al JOFET

The loop dimensions of the asymmetric SQUID used for CPR measurements have been chosen large enough to avoid Fraunhofer reduction in the flux range of interest (see S-III). The width of the loop arms is 10 μm and the associated self-inductance is estimated to be 102 pH. Its contribution to the measurement is negligible and discussed in S-II.

The total supercurrent I_{SQUID} flowing through the SQUID is the sum of the current flowing through each junction and thus includes the two current phase relations $I_w(\varphi_w)$ and $I_n(\varphi_n)$. Since one junction is much wider than the other, its critical current I_C^w is also much larger than that of the narrow junction I_C^n ($I_C^w/I_C^n = 15$). Thus, the maximum supercurrent through the SQUID is reached at $\varphi_w \approx \pi/2$ i.e. when the maximum current through J_w is reached. Taken into account the fluxoid relationship that relates the superconducting phases to the applied magnetic flux, the total critical current flux dependency of the SQUID can be written as :

$$I_C^{\text{SQUID}} = I_w(\pi/2) + I_n(\pi/2 + 2\pi\Phi_{\text{ext}}/\Phi_0) \quad (1)$$

where Φ_{ext} is the magnetic flux threading the loop and $\Phi_0 = h/2e$ the superconducting flux quantum.

One can clearly see that measuring the critical current

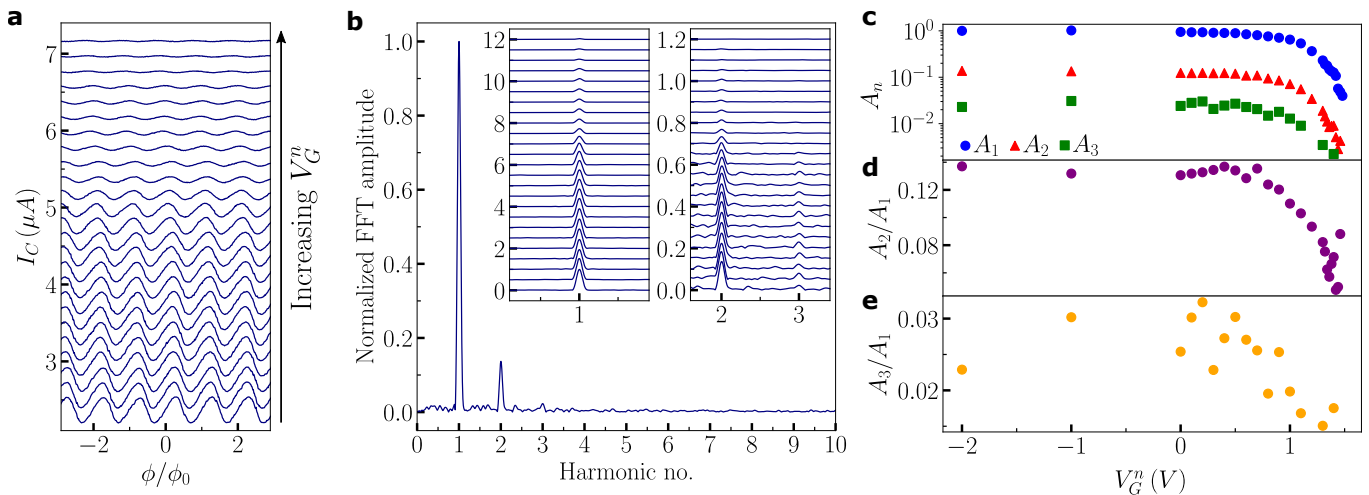


FIG. 2. **Gate modulation of the CPR harmonic content.** **a**, I_C modulations (shifted for clarity) of the asymmetric SQUID as a function of the flux for various V_G^n (each line correspond to one point in **c**, **d**, **e**) from full accumulation ($V_G^n = -2$ V) to near threshold ($V_G^n = 1.48$ V) with a fixed gate voltage applied to the wide junction ($V_G^w = -2$ V). **b**, Fast Fourier transform (FFT) (normalized to the first harmonic amplitude) of $I_C(\phi)$ at $V_G^n = -2$ V and, in the insets, for the same V_G^n range as in **a** (shifted for clarity). The three first harmonics are clearly visible and higher harmonics disappear faster when V_G^n gets close to the threshold voltage. **c**, Amplitude of the first three harmonics A_1 , A_2 and A_3 (in log scale) versus the gate voltage V_G^n . All of them tends to decrease with gate voltage since the overall flux modulation of I_C decreases. **d** [**e**], Ratio between the second [third] and the first harmonic amplitudes. The ratios decreasing highlights the disappearance of higher harmonics before the first one and thus a transition from a multi harmonics CPR toward a more sinusoidal one.

of the whole SQUID I_C^{SQUID} versus the applied flux Φ_{ext} allows to probe the current phase relation of the narrow junction J_n [23] (see S-III for details on the measurement protocol).

For this experiment, the wide junction J_w is kept in the full accumulation regime ($V_G^w = -2$ V). As expected, oscillations of the SQUID critical current are observed, as well as a background curvature associated to the Fraunhofer effect on the wide junction (S-III). The flux modulation $I_C(\Phi_{\text{ext}})$, studied for different values of the gate voltage V_G^n and shown in Fig. 2a after numerically removing the background, is a direct measurement of the CPR of the narrow junction.

One can already notice that $I_C(\Phi_{\text{ext}})$ is skewed in the highly accumulated regime suggesting the presence of higher harmonics. In order to better evidence the skewness and to quantify the various components of the CPR, we applied a Fourier transform to these data over 25 periods (Fig. 2b).

The spectral decomposition at full accumulation ($V_G^n = -2$ V) is shown in Fig. 2b. The result shows a clear contribution from the first and second harmonics, and also from the third harmonic but with less pronounced evidence. This confirms that the CPR is not purely sinusoidal. The insets of Fig. 2b show the gate dependence of the three harmonics. The first harmonic survives up to the largest gate voltages applied ($V_G^n = 1.48$ V) while the second and third harmonics vanish at a lower gate voltage.

The amplitude of the three first harmonics are extracted by taking the height of each peak in the Fourier

decomposition. A_n is the weight of the n^{th} harmonic and is plotted as a function of V_G^n in Fig. 2c. When V_G^n approaches the threshold voltage ($V_{th} \approx 1.5$ V), we observe a reduction of all harmonic amplitudes consistent with the reduction of the critical current. The ratio between A_2 (resp. A_3) and A_1 shown in Fig. 2d (resp. Fig. 2e) goes up to 0.13 (resp. 0.03). Interestingly, the gate dependence reveals the faster disappearance of higher harmonics compare to the main one. As mentioned above, higher harmonics in the CPR are intrinsic to the proximitized Josephson junctions. We have checked (see S-V) that multiple harmonics cannot originate from arm inductances as it is the case with S-I-S junctions. The faster disappearance of the higher harmonics reveals a change in the CPR as the proximitized Ge region gets depleted from carriers.

This is consistent with the decrease of the number of conduction channels (as the Fermi wavelength increases) leading to the reduction of the total non-dissipative current. Together, the Fermi velocity decreases and so is the proximity effect (through the reduction of penetration of Andreev pairs in the Ge channel). Moreover, the transmission coefficients of the conducting modes and the transparency of the S-Sm interfaces are affected by the reduction of carriers. All these effects contribute to decrease the probability of (multiple) transfer of Cooper pairs [14, 43].

IV. SHAPIRO STEPS IN A SINGLE Ge/Al JOFET

In the previous section, we have shown the results of the direct measurement of the CPR of the narrow junction. Thanks to the high gate control of our Ge based JoFET, the wide junction of the exact same SQUID device can be tuned in the very depleted regime at $V_G^w = 4\text{V}$ where the conductance is zero. The device is now only composed of the narrow junction for which the CPR is known.

In the following, we focus on the AC Josephson effect of the narrow junction, which should highlight the presence of higher harmonics in the CPR. Under microwave irradiation at frequency f , the current-voltage characteristic shows steps at some specific voltages $V = nhf/2e$ where h is the Plank constant, e the elementary charge and $n = 0,1,2,..$ called Shapiro steps [44]. If the CPR of the Josephson junction contains a second harmonic, half-integer Shapiro steps also appear ($n=1/2,3/2,..$) indicating the coherent transport of pairs of Cooper pairs through the junction (i.e. a charge-4e supercurrent)[45, 46].

Fig. 3a shows the differential resistance measurement (red line) and the measured DC voltage (blue line) as a function of the current bias under a radio-frequency irradiation at $f = 3.05\text{GHz}$ and with a fixed microwave power $P_{RF} = -12\text{dBm}$. We identify clear dips in the differential resistance that correspond to integer and half-integer Shapiro steps (highlighted by dashed grey lines).

Fig. 3b shows the differential resistance as a function of the microwave drive power P_{RF} and the DC bias I_{DC} . Dark regions correspond to dips in the differential resistance and are associated with Shapiro steps. The widths of these steps follow the usual Bessel-like behavior [47]. The clear observation of half-integer steps is perfectly consistent with previously measured harmonic content of the CPR.

By applying more positive gate voltages (V_G^n near threshold), one would expect half integer steps to disappear before integer ones as the CPR becomes purely sinusoidal. The quantitative analysis of this effect is challenging because of the overlap of the different step signals for such rounded steps. Shapiro patterns for different gate voltages are shown in S-IV.

As an intermediate conclusion, we have shown that proximitized planar SiGe based Josephson junctions exhibit intrinsic non purely sinusoidal current phase relation. This response has been probed and measured in a single junction, first in a SQUID geometry to directly measure the CPR and under radio-frequency irradiation to reveal half-integer Shapiro steps. This has been made possible thanks to the high gate tunability of the SiGe JoFETs.

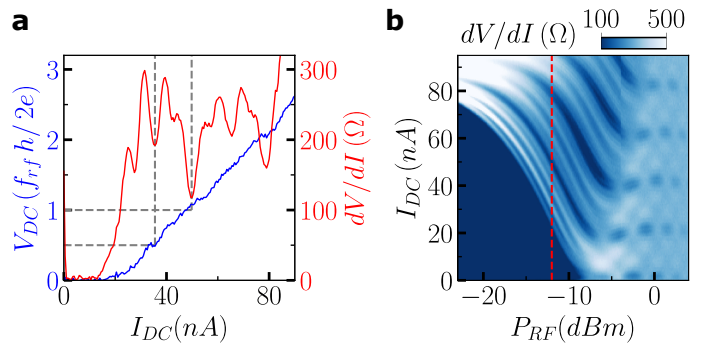


FIG. 3. **Integer and half-integer Shapiro steps.** **a**, DC voltage normalized to the expected Shapiro steps positions (blue line) and differential resistance (red line) as function of the bias current I_{DC} under radio-frequency irradiation at $f = 3.05\text{GHz}$ with a power $P_{RF} = -12\text{dBm}$ (see the dashed red line in **b**). The dashed grey lines are guides to the eye for the first half integer and integer steps. **b**, Differential resistance as function of the bias current I_{DC} as well as the microwave power P_{RF} . Integer (wide dark lines) and half-integer (narrow dark lines) follow the Bessel like oscillations as a function of the RF power.

V. SUPERCONDUCTING DIODE EFFECT IN A SYMMETRIC SQUID

In a SQUID with negligible arms inductances, superconducting diode effect (SDE) can still emerge if at least one of the junctions has a non-sinusoidal CPR [22, 24, 48]. To investigate this possibility, we have fabricated a SQUID with two nominally identical JoFETs, J_1 and J_2 with $W=4\mu\text{m}$ and $L=300\text{nm}$. The diode effect arises if (i) the external flux is not an integer multiple of the half flux quantum $\Phi = n\Phi_0/2$ and (ii) the two CPRs of the two junctions are not perfectly balanced. The SDE can be quantified through the diode efficiency:

$$\eta = \frac{I_C^+ - I_C^-}{I_C^+ + I_C^-} \quad (2)$$

where I_C^+ and I_C^- are the forward and backward critical currents of the SQUID.

Fig. 4a shows the diode efficiency η as a function of the gate voltage of J_1 (V_G^1) and the normalized flux Φ_{ext}/Φ_0 for a fixed value of $V_G^2 = 1.75\text{V}$ together with two $I_C^{+(-)}$ traces (Fig. 4c,d) from which the efficiency is calculated. As expected, the diode efficiency vanishes at half the flux quantum and follows very well the predicted behavior [24] with a maximum that goes up to 27%. At $V_G^1 = 1.825\text{V}$ (Fig. 4c) the diode efficiency drops to zero for any flux value. This suggests that for this combination of gate voltages the SQUID is perfectly symmetric. But this gate values combination is not unique.

To find every gate configurations that perfectly balance the SQUID, the device is flux-biased slightly below the half flux quantum ($\Phi_{ext} = 0.45\Phi_0$) and the diode

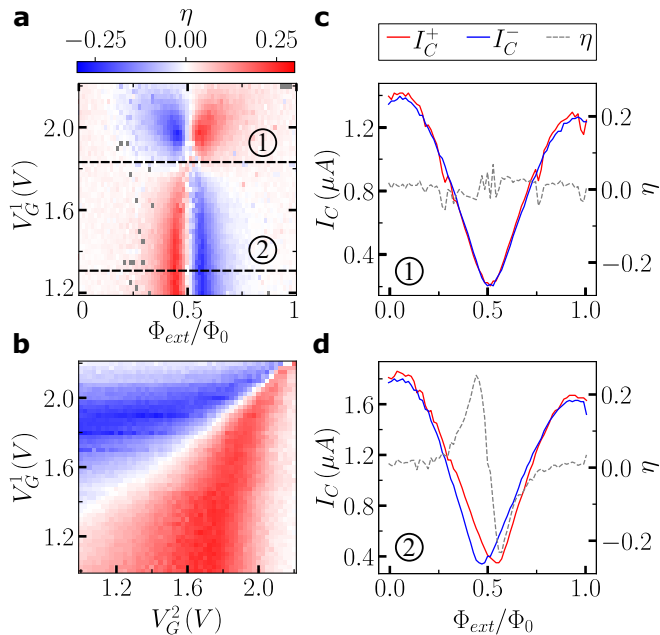


FIG. 4. **Gate and flux dependence of the superconducting diode effect.** **a**, Diode efficiency η as function of the normalized applied flux Φ_{ext}/Φ_0 and V_G^1 for a fixed $V_G^2 = 1.75$ V. η vanishes at half flux quantum $\Phi_{\text{ext}}/\Phi_0 = 0.5$ and for the peculiar gate voltage $V_G^1 = 1.825$ V. **b**, Diode efficiency as function of the two gate voltages V_G^1 and V_G^2 for a fixed flux biasing slightly below the half flux quantum $\Phi_{\text{ext}}/\Phi_0 = 0.45$. The white line corresponds to perfectly symmetric regime where the SDE disappears. **c,d** Forward I_C^+ (red line) and backward I_C^- (blue line) critical currents and extracted diode efficiency η as a function of the normalized applied flux Φ_{ext}/Φ_0 for $V_G^1 = 1.75$ V and $V_G^2 = 1.3$ V.

efficiency measured as a function of V_G^1 and V_G^2 . The result (Fig. 4b) highlights the existence of a line (in white) corresponding to all gate voltage combinations where the SQUID operates in a perfectly balanced regime. The critical current of the SQUID along this line is shown in S-VI. The fact that this line does not follow the $V_G^1 = V_G^2$ diagonal means that the two JoFETs have fairly close yet not identical characteristics. Nevertheless, the symmetric situation can be easily obtained thanks to the independent tunability of the junctions.

VI. SHAPIRO STEPS IN A PERFECTLY SYMMETRIC SQUID

In the previous section we have shown that the superconducting diode effect (SDE) observed in a symmetric SQUID is consistent with the non sinusoidal CPR of the junctions. We have also demonstrated that the contribution of the various harmonics strongly depends on the applied magnetic flux threading the SQUID. Moreover, as detailed before, DC Shapiro steps observed under radio-frequency irradiation can also reveal CPR multiple harmonics. In this section, we present the results of Shapiro

steps measured in the exact same SQUID than the one used to reveal SDE. To do so, we operate the SQUID for a fixed set of gate voltages $V_G^1 = 1.825$ V and $V_G^2 = 1.75$ V, which correspond to one of the symmetric regime combinations and vary the magnetic flux.

Fig. 5a is the theoretical amplitudes of the first and second harmonics as a function of the flux threading in a symmetric SQUID (see S-IX). Fig. 5b shows the differential resistance of the SQUID as a function of the applied external flux Φ_{ext} and the DC voltage V_{DC} normalized to the expected Shapiro steps positions, for a given microwave radiation power $P_{RF} = -8$ dBm and frequency $f = 7$ GHz. Dark blue ridges reveal the position of the Shapiro steps and evidence the emergence of half integer steps around $\Phi_0/2$. Fig. 5c,d,e show the differential resistance as a function of the microwave radiation power and the normalized DC voltage for three different fluxes $\Phi_{\text{ext}} = 0$, $\Phi_{\text{ext}} = \Phi_0/2$ and $\Phi_{\text{ext}} = \Phi_0/4$ corresponding to the dashed grey lines in Fig. 5a. At $\Phi_{\text{ext}} = \Phi_0$, both integer and half-integer steps are visible with a stronger intensity of the integer steps and follows the Bessel-type oscillations as a function of the power. At $\Phi_{\text{ext}} = \Phi_0/2$ integer and half-integer steps are still visible but with a relative contrast that is weaker than for $\Phi_{\text{ext}} = 0$. This reduction is consistent with the vanishing of the 1st harmonic at $\Phi_{\text{ext}} = \Phi_0/2$ but where integer steps correspond to a multiple photons process of half-integer steps. At $\Phi_{\text{ext}} = \Phi_0/4$ however, the contribution of the 2nd CPR harmonic vanishes and the half-integer steps disappear completely. Therefore, we demonstrated the flux-tunability of the 1st and 2nd harmonics opening the possibility to engineer a $\sin(2\varphi)$ Josephson element dominated by charge-4e supercurrent.

VII. CONCLUSION

In conclusion, our work harnesses the high gate tunability offered by SiGe-based proximitized Josephson junctions to conduct comprehensive measurements of the CPR and Shapiro steps within a single JoFET. The CPR clearly reveals gate-tunable non-purely sinusoidal phase dependence, revealing higher-order harmonics that correspond to the coherent transfer of both single and multiple Cooper pairs. This observation is supported by the presence of both integer and half integer Shapiro steps. We also revealed a gate and flux-tunable SDE in a SQUID geometry, made possible once again by the JoFETs high transparency and gate tunability [24]. Ultimately, we demonstrated the realization of a so-called $\sin(2\varphi)$ Josephson element in a SQUID biased at half flux quantum and finely gate-tuned to its balanced critical current point. Our results underscore the remarkable potential of the SiGe-based heterostructures for the realization of parity-protected superconducting qubits without the need for large inductance engineering as required with tunnel S-I-S junctions[18, 20, 49]. Our study focused on wide junctions, ranging from 1 to 10 μm , with critical

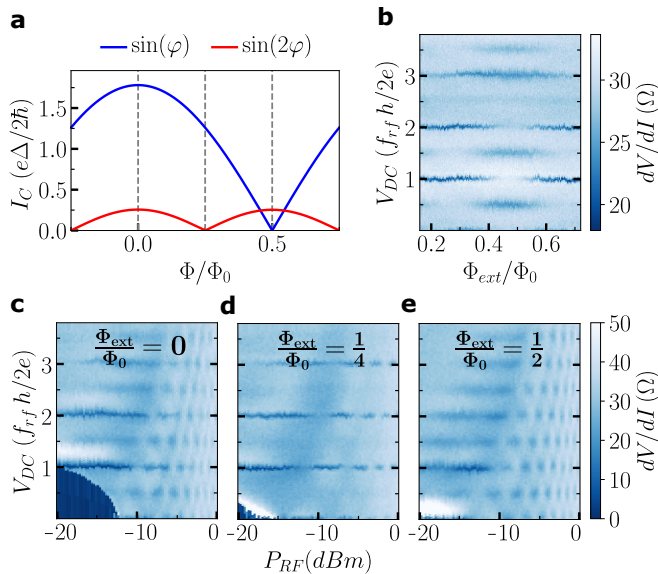


FIG. 5. **Half integer Shapiro steps as a probe for $\sin(2\varphi)$ CPR.** **a**, Computation of the two first harmonics amplitudes of a symmetric SQUID CPR for a single channel short junction model with a transparency $\tau = 0.7$ (see S-IX). **b**, Differential resistance as a function of the DC voltage V_{DC} normalized to the Shapiro steps expected positions and the applied flux normalized to ϕ_0 for a fixed $P_{RF} = -8$ dBm and in the balanced regime ($V_G^1 = 1.825$ V and $V_G^2 = 1.75$ V). Dark lines correspond to differential resistance dips associated to Shapiro steps. **b[d][e]**, Differential resistance as a function of the normalized DC voltage and the RF excitation power at fixed applied flux $\Phi_{ext} = 0$ [$\Phi_{ext} = \Phi_0/2$] [$\Phi_{ext} = \Phi_0/4$].

current spanning from a few hundred nA to a few μ A. These values suggest that narrower junctions, probably necessary to avoid Andreev bound states at low energies, will still have a large enough Josephson energy for the realization of suitable Gatemon qubits. Moreover, such materials are fully compatible with the CMOS technology and potentially large scale integration.

ACKNOWLEDGMENTS

This work has been supported by the ANR project SUNISIDEuP (ANR-19-CE47-0010), the PEPR ROBUSTSUPERQ (ANR-22-PETQ-0003), the ERC starting grant LONGSPIN (Horizon 2020 - 759388) and the Grenoble LaBEX LANEF. We thank Frederic Gustavo and Jean-Luc Thomassin for their contribution in the nanofabrication at the PTA (CEA-Grenoble) and the CNRS Neel Institute for the access to the Nanofab facility.

-
- [1] T. W. Larsen, K. D. Petersson, F. Kuemmeth, T. S. Jespersen, P. Krogstrup, J. Nygård, and C. M. Marcus, Semiconductor-Nanowire-Based Superconducting Qubit, *Physical Review Letters* **115**, 127001 (2015).
 - [2] G. de Lange, B. van Heck, A. Bruno, D. J. van Woerkom, A. Geresdi, S. R. Plissard, E. P. A. M. Bakkers, A. R. Akhmerov, and L. DiCarlo, Realization of Microwave Quantum Circuits Using Hybrid Superconducting-Semiconducting Nanowire Josephson Elements, *Physical Review Letters* **115**, 127002 (2015).
 - [3] L. Casparis, T. W. Larsen, M. S. Olsen, F. Kuemmeth, P. Krogstrup, J. Nygård, K. D. Petersson, and C. M. Marcus, Gatemon Benchmarking and Two-Qubit Operations, *Physical Review Letters* **116**, 150505 (2016).
 - [4] L. Casparis, M. R. Connolly, M. Kjaergaard, N. J. Pearson, A. Kringhøj, T. W. Larsen, F. Kuemmeth, T. Wang, C. Thomas, S. Gronin, G. C. Gardner, M. J. Manfra, C. M. Marcus, and K. D. Petersson, Superconducting gatemon qubit based on a proximitized two-dimensional electron gas, *Nature Nanotechnology* **13**, 915 (2018).
 - [5] J. I.-J. Wang, D. Rodan-Legrain, L. Bretheau, D. L. Campbell, B. Kannan, D. Kim, M. Kjaergaard, P. Krantz, G. O. Samach, F. Yan, J. L. Yoder, K. Watanabe, T. Taniguchi, T. P. Orlando, S. Gustavsson, P. Jarillo-Herrero, and W. D. Oliver, Coherent control of a hybrid superconducting circuit made with graphene-based van der Waals heterostructures, *Nature Nanotechnology* **14**, 120 (2019).
 - [6] G. Butseraen, A. Ranadive, N. Aparicio, K. R. Amin, A. Juyal, M. Esposito, K. Watanabe, T. Taniguchi, N. Roch, F. Lefloch, and J. Renard, A gate-tunable graphene Josephson parametric amplifier, *Nature Nanotechnology* **17**, 1153 (2022).
 - [7] J. Sarkar, K. V. Salunkhe, S. Mandal, S. Ghatak, A. H. Marchawala, I. Das, K. Watanabe, T. Taniguchi, R. Vijay, and M. M. Deshmukh, Quantum noise limited microwave amplification using a graphene Josephson junction, *Nature Nanotechnology* **17**, 1147 (2022).
 - [8] D. Phan, P. Falthansl-Scheinecker, U. Mishra, W. Strickland, D. Langone, J. Shabani, and A. Higginbotham, Gate-Tunable Superconductor-Semiconductor Parametric Amplifier, *Physical Review Applied* **19**, 064032 (2023).
 - [9] L. J. Splitthoff, J. J. Wesdorp, M. Pita-Vidal, A. Bargerbos, and C. K. Andersen, Gate-tunable kinetic inductance parametric amplifier, arXiv:2308.06989 [cond-mat, physics:quant-ph] (2023).
 - [10] W. M. Strickland, J. Lee, L. Baker, K. Dindial, B. H. Elfeky, M. Hatefipour, P. Yu, I. Levy, V. E. Manucharyan, and J. Shabani, Characterizing losses in InAs two-dimensional electron gas-based gatemon qubits, arXiv:2309.17273 [cond-mat, physics:quant-ph] (2023).

- [11] J. Huo, Z. Xia, Z. Li, S. Zhang, Y. Wang, D. Pan, Q. Liu, Y. Liu, Z. Wang, Y. Gao, J. Zhao, T. Li, J. Ying, R. Shang, and H. Zhang, Gate-mon Qubit Based on a Thin InAs-Al Hybrid Nanowire, *Chinese Physics Letters* **40**, 047302 (2023).
- [12] A. Hertel, M. Eichinger, L. O. Andersen, D. M. van Zanten, S. Kallatt, P. Scarlino, A. Kringhøj, J. M. Chavez-Garcia, G. C. Gardner, S. Gronin, M. J. Manfra, A. Geynis, M. Kjaergaard, C. M. Marcus, and K. D. Petersson, Gate-Tunable Transmon Using Selective-Area-Grown Superconductor-Semiconductor Hybrid Structures on Silicon, *Physical Review Applied* **18**, 034042 (2022).
- [13] E. Zhuo, Z. Lyu, X. Sun, A. Li, B. Li, Z. Ji, J. Fan, E. P. a. M. Bakkers, X. Han, X. Song, F. Qu, G. Liu, J. Shen, and L. Lu, Hole-type superconducting gate-mon qubit based on Ge/Si core/shell nanowires, *npj Quantum Information* **9**, 1 (2023).
- [14] W. Haberkorn, H. Knauer, and J. Richter, A theoretical study of the current-phase relation in Josephson contacts, *physica status solidi (a)* **47**, K161 (1978).
- [15] E. M. Spanton, M. Deng, S. Vaitiekėnas, P. Krogstrup, J. Nygård, C. M. Marcus, and K. A. Moler, Current-phase relations of few-mode InAs nanowire Josephson junctions, *Nature Physics* **13**, 1177 (2017).
- [16] S. Gladchenko, D. Olaya, E. Dupont-Ferrier, B. Douçot, L. B. Ioffe, and M. E. Gershenson, Superconducting nanocircuits for topologically protected qubits, *Nature Physics* **5**, 48 (2009).
- [17] B. Douçot and L. B. Ioffe, Physical implementation of protected qubits, *Reports on Progress in Physics* **75**, 072001 (2012).
- [18] W. C. Smith, A. Kou, X. Xiao, U. Vool, and M. H. Devoret, Superconducting circuit protected by two-Cooper-pair tunneling, *npj Quantum Information* **6**, 1 (2020).
- [19] W. C. Smith, M. Villiers, A. Marquet, J. Palomo, M. R. Delbecq, T. Kontos, P. Campagne-Ibarcq, B. Douçot, and Z. Leghtas, Magnifying quantum phase fluctuations with Cooper-pair pairing, *Physical Review X* **12**, 021002 (2022).
- [20] T. W. Larsen, M. E. Gershenson, L. Casparis, A. Kringhøj, N. J. Pearson, R. P. G. McNeil, F. Kuemmeth, P. Krogstrup, K. D. Petersson, and C. M. Marcus, Parity-Protected Superconductor-Semiconductor Qubit, *Physical Review Letters* **125**, 056801 (2020).
- [21] C. Ciaccia, R. Haller, A. C. C. Drachmann, T. Lindemann, M. J. Manfra, C. Schrade, and C. Schönenberger, Charge-4e supercurrent in an InAs-Al superconductor-semiconductor heterostructure, *arXiv:2306.05467 [cond-mat]* (2023).
- [22] M. Valentini, O. Sagi, L. Baghumyan, T. de Gijssel, J. Jung, S. Calcaterra, A. Ballabio, J. A. Servin, K. Aggarwal, M. Janik, T. Adletzberger, R. S. Souto, M. Leijnse, J. Danon, C. Schrade, E. Bakkers, D. Christina, G. Isella, and G. Katsaros, Parity-conserving Cooper-pair transport and ideal superconducting diode in planar Germanium, *arXiv:2306.07109 [cond-mat]* (2023).
- [23] M. L. Della Rocca, M. Chauvin, B. Huard, H. Pothier, D. Esteve, and C. Urbina, Measurement of the Current-Phase Relation of Superconducting Atomic Contacts, *Physical Review Letters* **99**, 127005 (2007).
- [24] R. S. Souto, M. Leijnse, and C. Schrade, Josephson Diode Effect in Supercurrent Interferometers, *Physical Review Letters* **129**, 267702 (2022).
- [25] F. Ando, Y. Miyasaka, T. Li, J. Ishizuka, T. Arakawa, Y. Shiota, T. Moriyama, Y. Yanase, and T. Ono, Observation of superconducting diode effect, *Nature* **584**, 373 (2020).
- [26] L. Bauriedl, C. Bäuml, L. Fuchs, C. Baumgartner, N. Paulik, J. M. Bauer, K.-Q. Lin, J. M. Lupton, T. Taniguchi, K. Watanabe, C. Strunk, and N. Paradiso, Supercurrent diode effect and magnetochiral anisotropy in few-layer NbSe₂, *Nature Communications* **13**, 4266 (2022).
- [27] A. Daido, Y. Ikeda, and Y. Yanase, Intrinsic Superconducting Diode Effect, *Physical Review Letters* **128**, 037001 (2022).
- [28] J. Yun, S. Son, J. Shin, G. Park, K. Zhang, Y. J. Shin, J.-G. Park, and D. Kim, Magnetic proximity-induced superconducting diode effect and infinite magnetoresistance in a van der Waals heterostructure, *Physical Review Research* **5**, L022064 (2023).
- [29] S. Ilić and F. S. Bergeret, Theory of the Supercurrent Diode Effect in Rashba Superconductors with Arbitrary Disorder, *Physical Review Letters* **128**, 177001 (2022).
- [30] J. J. He, Y. Tanaka, and N. Nagaosa, A phenomenological theory of superconductor diodes, *New Journal of Physics* **24**, 053014 (2022).
- [31] S. Matsuo, T. Imoto, T. Yokoyama, Y. Sato, T. Lindemann, S. Gronin, G. C. Gardner, M. J. Manfra, and S. Tarucha, Josephson diode effect derived from short-range coherent coupling, *Nature Physics* , 1 (2023).
- [32] T. Yokoyama, M. Eto, and Y. V. Nazarov, Anomalous Josephson effect induced by spin-orbit interaction and Zeeman effect in semiconductor nanowires, *Physical Review B* **89**, 195407 (2014).
- [33] A. Zazunov, R. Egger, T. Jonckheere, and T. Martin, Anomalous Josephson Current through a Spin-Orbit Coupled Quantum Dot, *Physical Review Letters* **103**, 147004 (2009).
- [34] K. Halterman, M. Alidoust, R. Smith, and S. Starr, Supercurrent diode effect, spin torques, and robust zero-energy peak in planar half-metallic trilayers, *Physical Review B* **105**, 104508 (2022).
- [35] E. Strambini, M. Spies, N. Ligato, S. Ilić, M. Rouco, C. González-Orellana, M. Ilyn, C. Rogero, F. S. Bergeret, J. S. Moodera, P. Virtanen, T. T. Heikkilä, and F. Giazotto, Superconducting spintronic tunnel diode, *Nature Communications* **13**, 2431 (2022).
- [36] S. Pal and C. Benjamin, Quantized Josephson phase battery, *Europhysics Letters* **126**, 57002 (2019).
- [37] J.-M. Hartmann, N. Bernier, F. Pierre, J.-P. Barnes, V. Mazzocchi, J. Krawczyk, G. Lima, E. Kiyooka, and S. D. Franceschi, Epitaxy of Group-IV Semiconductors for Quantum Electronics, *ECS Transactions* **111**, 53 (2023).
- [38] N. W. Hendrickx, M. L. V. Tagliaferri, M. Kouwenhoven, R. Li, D. P. Franke, A. Sammak, A. Brinkman, G. Scappucci, and M. Veldhorst, Ballistic supercurrent discretization and micrometer-long Josephson coupling in germanium, *Physical Review B* **99**, 075435 (2019).
- [39] F. Vigneau, R. Mizokuchi, D. C. Zanuz, X. Huang, S. Tan, R. Maurand, S. Frolov, A. Sammak, G. Scappucci, F. Lefloch, and S. De Franceschi, Germanium Quantum-Well Josephson Field-Effect Transistors and Interferometers, *Nano Letters* **19**, 1023 (2019).
- [40] K. Aggarwal, A. Hofmann, D. Jirovec, I. Prieto, A. Sammak, M. Botifoll, S. Martí-Sánchez, M. Veldhorst, J. Ar-

- biol, G. Scappucci, J. Danon, and G. Katsaros, Enhancement of proximity-induced superconductivity in a planar Ge hole gas, *Physical Review Research* **3**, L022005 (2021).
- [41] A. Tosato, V. Levajac, J.-Y. Wang, C. J. Boor, F. Borsoi, M. Botifoll, C. N. Borja, S. Martí-Sánchez, J. Arbiol, A. Sammak, M. Veldhorst, and G. Scappucci, Hard superconducting gap in germanium, *Communications Materials* **4**, 1 (2023).
- [42] J. Xiang, A. Vidan, M. Tinkham, R. M. Westervelt, and C. M. Lieber, Ge/Si nanowire mesoscopic Josephson junctions, *Nature Nanotechnology* **1**, 208 (2006).
- [43] A. A. Golubov, M. Y. Kupriyanov, and E. Il'ichev, The current-phase relation in Josephson junctions, *Reviews of Modern Physics* **76**, 411 (2004).
- [44] S. Shapiro, Josephson Currents in Superconducting Tunneling: The Effect of Microwaves and Other Observations, *Physical Review Letters* **11**, 80 (1963).
- [45] K. Ueda, S. Matsuo, H. Kamata, Y. Sato, Y. Takeshige, K. Li, L. Samuelson, H. Xu, and S. Tarucha, Evidence of half-integer Shapiro steps originated from nonsinusoidal current phase relation in a short ballistic InAs nanowire Josephson junction, *Physical Review Research* **2**, 033435 (2020).
- [46] A. Iorio, A. Crippa, B. Turini, S. Salimian, M. Carrega, L. Chirulli, V. Zannier, L. Sorba, E. Strambini, F. Giazotto, and S. Heun, Half-integer Shapiro steps in highly transmissive InSb nanoflag Josephson junctions, *Physical Review Research* **5**, 033015 (2023).
- [47] P. Russer, Influence of Microwave Radiation on Current-Voltage Characteristic of Superconducting Weak Links, *Journal of Applied Physics* **43**, 2008 (1972).
- [48] C. Ciaccia, R. Haller, A. C. C. Drachmann, T. Lindemann, M. J. Manfra, C. Schrade, and C. Schönenberger, Gate-tunable Josephson diode in proximitized InAs supercurrent interferometers, *Physical Review Research* **5**, 033131 (2023).
- [49] C. Schrade, C. M. Marcus, and A. Gyonis, Protected Hybrid Superconducting Qubit in an Array of Gate-Tunable Josephson Interferometers, *PRX Quantum* **3**, 030303 (2022).
- [50] F. Lecocq, *Dynamique Quantique Dans Un dcSQUID : Du Qubit de Phase à l'oscillateur Quantique Bidimensionnel*, These de doctorat, Grenoble (2011).
- [51] E. Dumur, *A V-shape Superconducting Artificial Atom for Circuit Quantum Electrodynamics*, These de doctorat, Université Grenoble Alpes (ComUE) (2015).
- [52] C. W. J. Beenakker and H. Van Houten, Josephson current through a superconducting quantum point contact shorter than the coherence length, *Physical Review Letters* **66**, 3056 (1991).
- [53] D. C. Mattis and J. Bardeen, Theory of the Anomalous Skin Effect in Normal and Superconducting Metals, *Physical Review* **111**, 412 (1958).
- [54] M. Tinkham, *Introduction to Superconductivity*, 2nd ed., Dover Books on Physics (Dover Publ, Mineola, NY, 2015).
- [55] D. S. Holmes and J. McHenry, Non-normal Critical Current Distributions in Josephson Junctions With Aluminum Oxide Barriers, *IEEE Transactions on Applied Superconductivity* **27**, 1 (2017).
- [56] P. Dubos, H. Courtois, O. Buisson, and B. Pannetier, Coherent Low-Energy Charge Transport in a Diffusive S-N-S Junction, *Physical Review Letters* **87**, 206801 (2001).
-

Supplemental Materials

S-I. ASYMMETRIC SQUID CRITICAL CURRENT AND NORMAL RESISTANCE

The critical current is defined as the switching current from the superconducting to the normal state. The data presented in Fig. S1 have been measured at a not optimized perpendicular magnetic field, and explain the I_C reduction compared to those in the main text. The normal resistances are measured at large bias ($eV_{Bias} > 3\Delta_{Al}$).

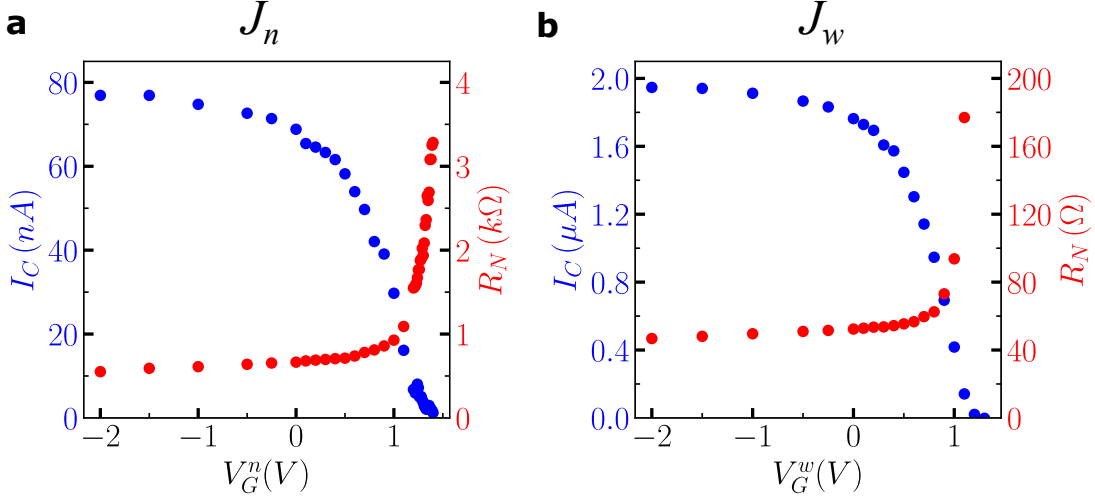


FIG. S1. **Critical current and normal resistance of J^n and J^w .** **a** The data for the narrow junction J^n ($W=1\ \mu\text{m}$ and $L=300\ \text{nm}$). **b** The data for the wide junction J^w ($W=8\ \mu\text{m}$ and $L=300\ \text{nm}$).

S-II. MODEL INCLUDING LOOP INDUCTANCE

We describe a way of computing the critical current of a SQUID made up of JJs with a multi-harmonics CPR and taking into account the inductances of each arms of the loop. The method is adapted from [50, 51].

For simplicity, the CPR of a single junction is defined as follows [52]:

$$I(\varphi) = I_C \frac{\bar{\tau} \sin(\varphi)}{\sqrt{1 - \bar{\tau} \sin^2(\varphi/2)}} \quad (\text{S1})$$

where I_C is the critical current, $\bar{\tau}$ is the junction main transparency and φ its phase. Although not strictly correct, such description allows to capture the multiple harmonics dependence of the CPR with limited parameters. The corresponding Josephson energy is then written:

$$E_J(\varphi) = I_C \frac{2\hbar}{e} \sqrt{1 - \bar{\tau} \sin^2(\varphi/2)} \quad (\text{S2})$$

In the SQUID, the two junctions phase differences respect the condition:

$$\varphi_n - \varphi_w = 2\pi \frac{\Phi}{\Phi_0} \quad (\text{S3})$$

where φ_w and φ_n are the phase differences across the two junctions, Φ_0 the flux quantum, Φ is the flux through the SQUID loop.

Furthermore, the two arms loop inductances L_1 and L_2 (as described in Fig. S2) induce a flux screening of the applied external flux Φ_{ext} so that:

$$\Phi = \Phi_{\text{ext}} + I_{\text{screen}}(L_1 + L_2) \quad (\text{S4})$$

where I_{screen} is the screening current flowing in the SQUID loop:

$$I_{\text{screen}} = \frac{1}{L_1 + L_2} \left[\frac{\Phi_0}{2\pi} (\varphi_n - \varphi_w) - \Phi_{\text{ext}} \right] \quad (\text{S5})$$

Thus, the inductance energy stored in each arm is:

$$E_{L_1} = \frac{1}{2} L_1 \left(\frac{I_B}{2} + I_{\text{screen}} \right)^2 \quad E_{L_2} = \frac{1}{2} L_2 \left(\frac{I_B}{2} - I_{\text{screen}} \right)^2 \quad (\text{S6})$$

where I_B is the applied bias current. Also, the junctions driven energy are written as follows:

$$E_B^w = -I_B \left(\frac{\Phi_0}{2\pi} \right) \varphi_w \quad E_B^n = -I_B \left(\frac{\Phi_0}{2\pi} \right) \varphi_n \quad (\text{S7})$$

and the total SQUID potential energy can be written as the sum of all the previously derived contributions:

$$U = -E_J^w - E_J^n - E_B^w - E_B^n - E_{L_1} - E_{L_2} \quad (\text{S8})$$

We define the new phase coordinates x and y respectively for the symmetric and anti-symmetric modes:

$$x = \frac{\varphi_w + \varphi_n}{2} \quad y = \frac{\varphi_w - \varphi_n}{2} \quad (\text{S9})$$

and introduce the circuit parameters and the normalized bias current:

$$\alpha = \frac{I_C^w - I_C^n}{I_C^w + I_C^n} \quad \eta = \frac{L_2 - L_1}{L_1 + L_2} \quad \beta = \frac{L_1 + L_2}{\Phi_0/2\pi(I_C^w + I_C^n)} \quad s = \frac{2I_B}{I_C^w + I_C^n} \quad (\text{S10})$$

Finally, assuming identical mean transparency $\bar{\tau}$ in each junction, we get the full expression for the potential:

$$U(x, y) = U_0 \left[s(x + \eta y) \Phi_0^2 - \frac{1}{\beta} (\Phi_0 y - \pi \Phi_{\text{ext}})^2 + \sqrt{2} \Phi_0^2 \left((1 + \alpha) \sqrt{2 - \bar{\tau} + \bar{\tau} \cos(x - y)} \right. \right. \\ \left. \left. + (1 - \alpha) \sqrt{2 - \bar{\tau} + \bar{\tau} \cos(x + y)} \right) \right]$$

For a given Φ_{ext} and I_B , the potential U consist in wells separated by saddle points. When I_B reaches the critical current, these potential wells does not represent stable position any longer. This situation can be described by the following conditions:

$$\begin{cases} \partial_x U(x, y, s) & = 0 \\ \partial_y U(x, y, s) & = 0 \\ \partial_{xx} U(x, y, s) \partial_{yy} U(x, y, s) - \partial_{xy} U(x, y, s) \partial_{yx} U(x, y, s) & = 0 \end{cases} \quad (\text{S11})$$

In what follows, the critical current as a function of the external flux is calculated by numerically solving S11.

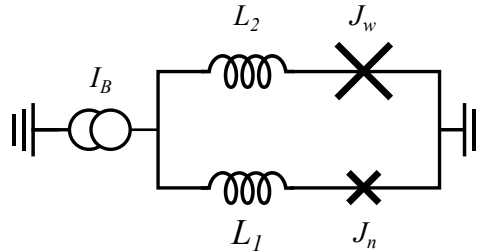


FIG. S2. **Equivalent circuit of the SQUID including arm inductances.** J_n and J_w are the narrow and the wide junctions, L_1 and L_2 are the inductances of the two arms of the SQUID. The SQUID is current biased by I_B .

The inductances L_1 and L_2 have a geometric and a kinetic contribution L_{geo} and L_{kin} . The kinetic inductance per square L_{kin}^S is estimated from the aluminum normal state sheet resistance $R_S = 1 \Omega$ and its superconducting critical temperature $T_C = 1.54 \text{ K}$ [53, 54]:

$$L_{\text{kin}}^S \approx \frac{\hbar}{\pi} \frac{R_S}{1.76 k_B T_C} \quad (\text{S12})$$

where k_B is the Boltzmann constant. We find $L_{\text{kin}}^S = 1 \text{ pH sq}^{-1}$. To estimate the total loop inductance $L = L_{\text{kin}} + L_{\text{geo}}$, we use a finite elements simulation performed in Sonnet and find $L = 102 \text{ pH}$. The contribution of the SQUID arm containing the small (resp. wide) junction is $L_1 = 50 \text{ pH}$ (resp. $L_2 = 52 \text{ pH}$). Thus the characteristic parameters of the SQUID are:

$$\beta = \frac{L}{\Phi_0/2\pi I_C} = 0.64 \quad \eta = \frac{L_2 - L_1}{L_1 + L_2} = 0.02 \quad (\text{S13})$$

The SQUID loop inductance and the presence of higher harmonics in the junction CPR may both lead to skewness in the I_C versus Φ data. To discriminate their respective contributions in our measurements we use the model described above where both contributions are taken into account. In all the following fits, the wide junction critical current is set to $I_C^w = 2.39 \text{ }\mu\text{A}$ according to Fig. S4d and the data used correspond to the $V_G^n = V_G^w = -2 \text{ V}$ configuration.

First, the transparency is fixed to zero meaning that we consider the sinusoidal CPR regime for the two junctions. The arms inductances are set to the values calculated with Sonnet and I_C^n is the only free parameter. The fit, shown in Fig. S3a, results in a $\chi^2 = 3.8 \times 10^{10}$ and the CPR skewness can poorly be reproduced with this loop inductance values.

Second, Fig. S3b shows the same fit except that the inductances are free parameters. The fit results in a $\chi^2 = 1.3 \times 10^{10}$ and the CPR skewness can be reproduced taking a tremendous and asymmetric loop inductance, $L_1 = 1.08 \text{ nH}$ and $L_2 < 50 \text{ pH}$. However, this inductance is completely at odds with the Sonnet simulations.

Third, Fig. S3c shows a parameter set reproducing the CPR skewness where the inductances are set to the values calculated before and where the junctions CPR are modeled by the SNS short junction theory (S1). The average transparency $\bar{\tau}$ and I_C^n were the only free parameters and $\chi^2 = 1.4 \times 10^{10}$.

To conclude, the SQUID loop inductance cannot by itself explain the data and the use of a multi harmonics CPR model is required to reproduce the observed skewness.

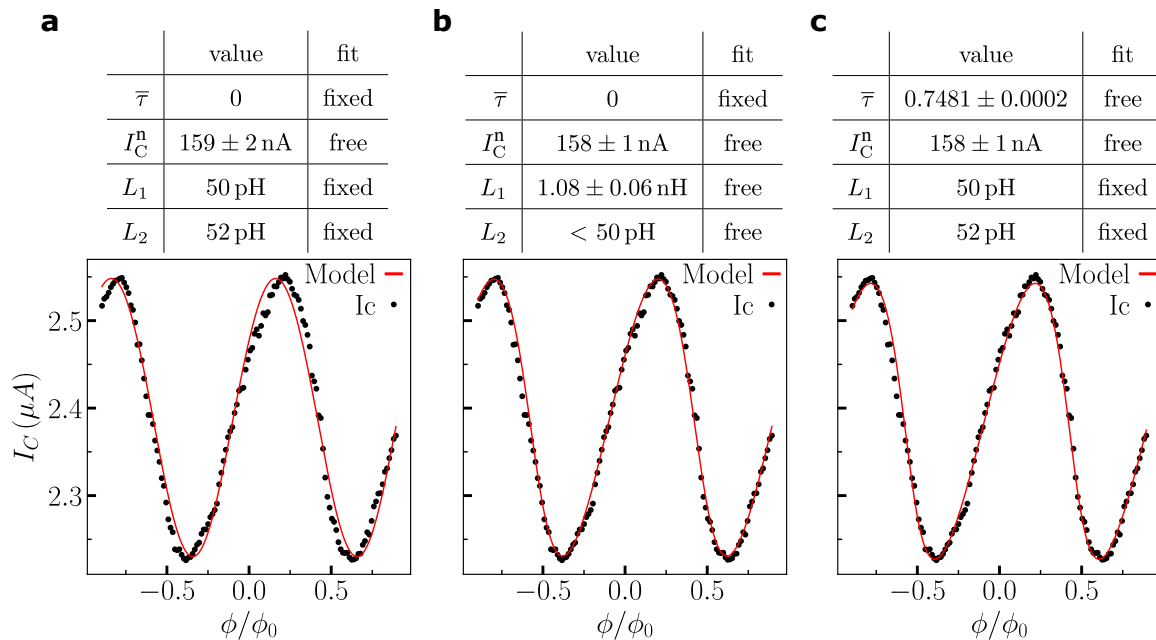


FIG. S3. CPR data fitting taking the SQUID loop inductance into account. **a**, The junctions CPR are sinusoidal, the loop inductance is set to the value calculated with Sonnet and I_C^n is the only fitting parameter. **b**, The junctions CPR are sinusoidal, the two arms inductances L_1 and L_2 and I_C^n are the fitting parameters. **c**, The loop inductance is set to the value calculated with Sonnet, the junctions CPR follows the SNS short junction model, their transparency $\bar{\tau}$ and I_C^n are the fitting parameters.

S-III. CRITICAL CURRENT STATISTICS

In Fig. S2a,b,c,d, each measured critical current is represented by a black spot, 100 I_C measurements are performed for each flux value Φ . The wide junction gate voltage is kept at $V_G^w = -2$ V while the small junction gate voltage is $V_G^n = -2$ V in **a**, $V_G^n = 1.1$ V in **b**, $V_G^n = 1.3$ V in **c**, $V_G^n = 1.5$ V in **d**. The oscillations are due to the SQUID effect and associated with the small junction CPR, they disappear near pinch-off (i.e. when V_G^n is near $V_{th} \approx 1.5$ V). The background curvature is associated with the Fraunhofer effect and is independent from V_G^n . Fig. S2e shows a zoom in around $\Phi = 0$ at $V_G^n = -2$ V. The I_C distributions at $\Phi/\Phi_0 = -0.3$, $\Phi/\Phi_0 = 0$ and $\Phi/\Phi_0 = 0.28$ are shown in the right panel. In Fig. S2f, A Shapiro-Wilk test for normality is performed on the I_C distribution at each flux value for $V_G^n = -2$ V. The resulting p-values are plotted as a function of the applied flux. The normality of the I_C distribution appears to be uncorrelated with the applied flux. The right panel shows the distribution of the Shapiro-Wilk p-values. We notice that for 82.5% of the Φ values the p-value is below the usual threshold (5.10^{-2}), indicating the non normality of the I_C distribution for these flux values. In Fig. S2g, for $V_G^n = -2$ V, the standard deviation σ of the I_C distribution is plotted as a function of the applied flux. The standard deviation appears to be uncorrelated with the applied flux. The right panel shows the σ distribution for all Φ values. In Fig. S2h, the average standard deviation $\bar{\sigma}$ as function of the small junction gate voltage V_G^n is plotted in yellow. The $\bar{\sigma}$ does not vary by more than 2% over the entire gate voltage range meaning that the critical current dispersion amplitude is not correlated with the small junction gate voltage value V_G^n . At each gate voltage V_G^n , the Shapiro-Wilk test for normality is performed for each flux and the fraction of p-values found to be above the 5.10^{-2} threshold is reported in purple. Again, this quantity does not vary by more than 5% over the entire V_G^n range, implying that the nature of the I_C distribution is not correlated with the applied V_G^n . However, the fact that the critical current distribution does not follow a normal law has already been reported [55], but in our case is probably due to the measurement technique (using a counter without signal integration). The detection of the normal state resistance transition is sensitive to low current false positives induced by noise above the detection threshold in the measured voltage.

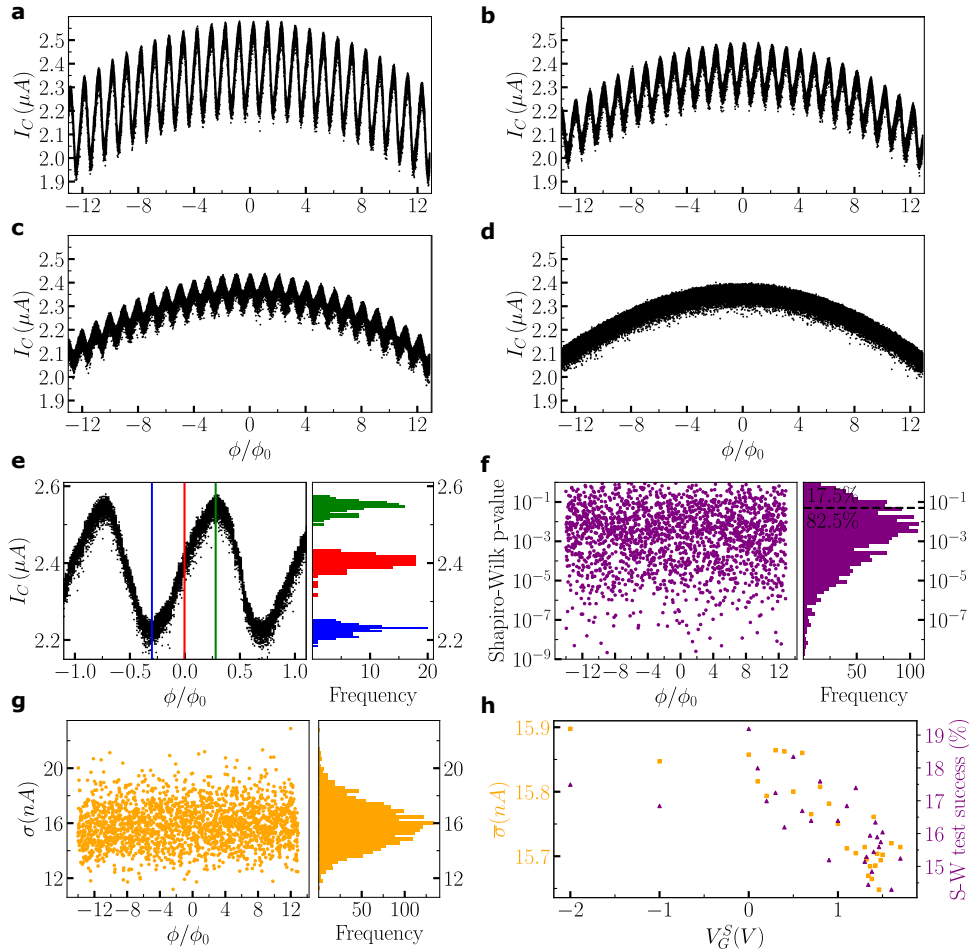


FIG. S4. Asymmetric SQUID raw critical current data and statistical analysis.

S-IV. SHAPIRO PATTERN AT DIFFERENT GATE VOLTAGES AND TEMPERATURES

The measurement of part IV is reproduced at different V_G^n keeping the wide junction in depletion ($V_G^w = 4$ V). Fig. S5 shows the different Shapiro patterns at various V_G^n with $f = 3.05$ GHz. The higher harmonics of the CPR disappear when the gate voltage is close to the threshold voltage ($V_{th} \approx 1.5$ V) (see Sec. III). Thus, one can expect the half integer steps to disappear before the integer ones when V_G^n gets close to the threshold. A rigorous quantitative analysis of such a phenomenon is challenging in this system because the Shapiro steps are rounded. In fact, the signatures of the half-integer and integer steps in the dV/dI measurement often overlap and mix, especially near threshold.

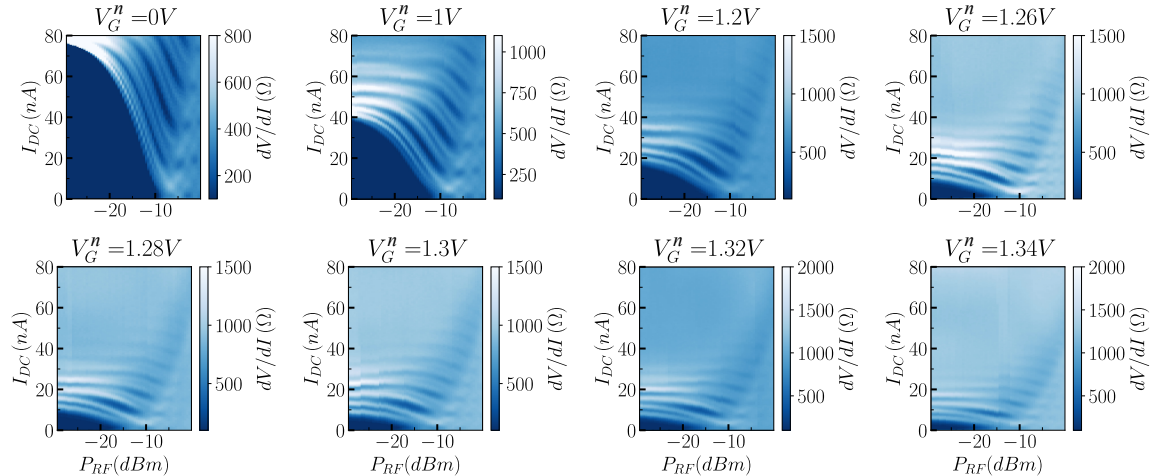


FIG. S5. **Shapiro pattern of the asymmetric SQUID small junction at different gate voltages.** The wide junction is kept in depletion ($V_G^w = 4$ V) so that the small junction is the only one to be probed. The experimental setup is the same as in part IV with $f = 3.05$ GHz and here the measurement is reproduced at different V_G^n .

Then, we investigate the temperature dependence of the small junction Shapiro pattern in the accumulation regime ($V_G^n = -2$ V and $V_G^w = 4$ V). Fig. S6 shows the different Shapiro patterns at various temperatures with $f = 3.05$ GHz. As the temperature increases, the Shapiro steps signatures in the dV/dI are broadened and blurred. There is no clear enhancement of the half-integer steps with increasing temperature, which could be associated with an out-of-equilibrium effect [56].

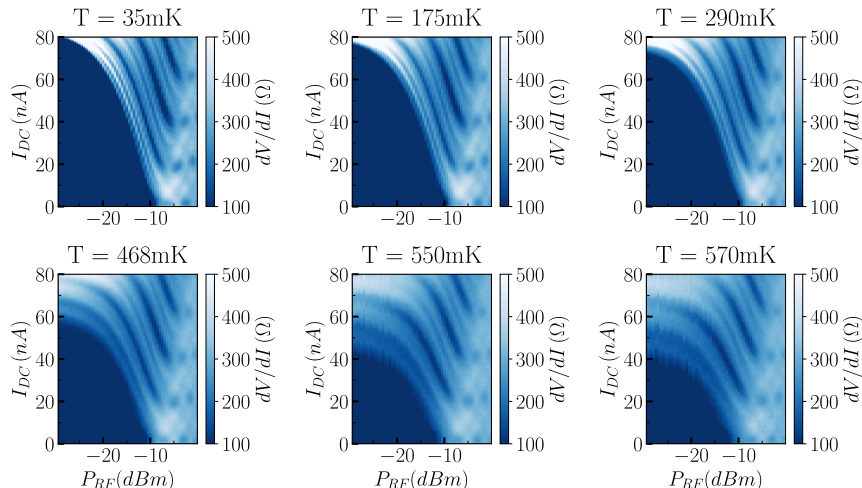


FIG. S6. **Shapiro pattern of the asymmetric SQUID small junction at various temperatures.** The wide junction is kept in depletion ($V_G^w = 4$ V) so that the small junction (kept in accumulation $V_G^n = -2$ V) is the only one to be probed. The experimental setup is the same as in part IV with $f = 3.05$ GHz and the measurement is reproduced at different temperatures.

S-V. SQUID EFFECT OSCILLATIONS IN THE SYMMETRIC DEVICE

The usual SQUID effect oscillations are observed in the symmetric SQUID device where J_1 and J_2 are $W=1\mu\text{m}$ wide and $L=300\text{nm}$ long. The SQUID effect experiment is performed with the two junctions in accumulation ($V_G^1 = V_G^2 = -1\text{V}$). In Fig. S7a, we show the measured voltage as a function of the bias current and the applied magnetic flux Φ_{ext} . The red dotted line follows the critical current I_C defined by a threshold voltage $V_{th} = 1.5\mu\text{V}$. The periodicity of the I_C maxima and minima is used to calibrate the relationship between the applied perpendicular magnetic field and the magnetic flux through the SQUID. Furthermore, the more balanced the SQUID is (i.e. the critical currents of the two junctions are equal), the lower I_C will be at half the flux quantum ($\Phi_{ext}/\Phi_0 = 0.5$). Thus, one way to find the gate voltage combinations that allow reaching the symmetric regime is to try to minimize I_C at $\Phi_{ext}/\Phi_0 = 0.5$. In Fig. S7b, we show the measured voltage as a function of the bias current and the J_1 gate voltage V_G^1 . The applied flux is held at half the flux quantum and $V_G^2 = 1\text{V}$. The red dotted line follows I_C defined as before. The minimum I_C is reached at $V_G^1 \approx 1.4\text{V}$ which means that the SQUID is operated in a symmetric regime for the gate combination $V_G^1 = 1.4\text{V}$ & $V_G^2 = 1\text{V}$. This result is consistent with the Fig. 4d where we see that this gate combination is one of the possibilities to reach the balanced SQUID regime.

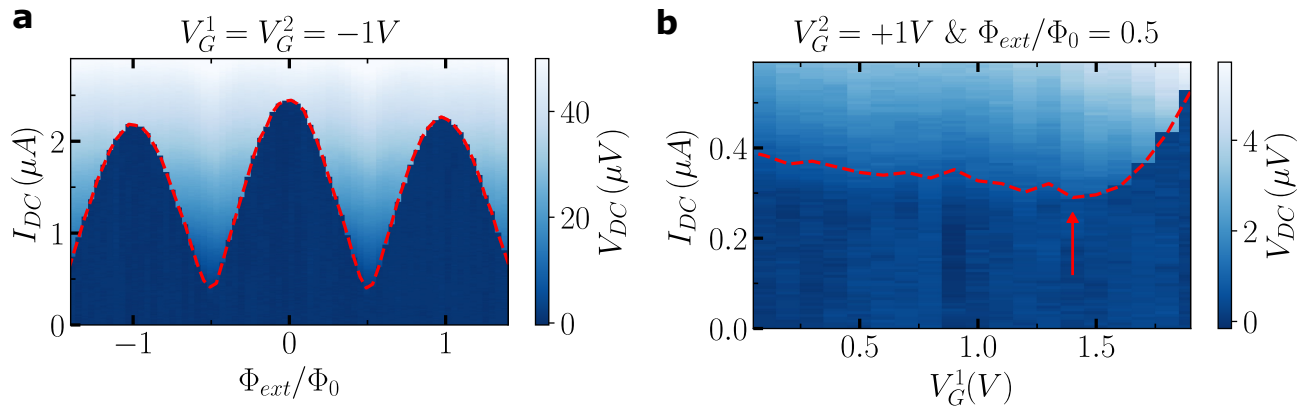


FIG. S7. **Symmetric SQUID oscillations and I_C minimization at half the flux quantum.** **a**, Measured voltage V_{DC} as a function of the bias current I_{DC} and the applied magnetic flux Φ_{ext} . The two gate voltages are kept at -1V . The red dotted line follows the critical current I_C defined by a voltage threshold $V_{th} = 1.5\mu\text{V}$. **b**, Measured voltage as a function of the bias current and the J_1 gate voltage V_G^1 while the applied magnetic flux is held at half flux quantum and $V_G^2 = 1\text{V}$. The red dotted line follows I_C defined as before and the red arrow points its minimum where the balanced SQUID regime is reached.

S-VI. CRITICAL CURRENT IN THE BALANCED SQUID REGIME

In Fig. S8a we show the diode efficiency η at fixed applied flux $\Phi_{ext}/\Phi_0 = 0.45$ (same as in Fig. 4d). When the SQUID is balanced, the diode efficiency goes to zero and so the line is defined by the diode efficiency minima and marked by the black crosses. The SQUID critical current I_C along this line is plotted on Fig. S8b as a function of the two gate voltages. I_C decreases as the gate voltages approach pinch-off. The I_C abrupt fluctuations are not related to gate voltage fluctuations since there is not such pattern in the sweet line versus gates (Fig. S8a). Magnetic flux fluctuations smaller than $\Phi_0/20$ could explain the phenomenon.

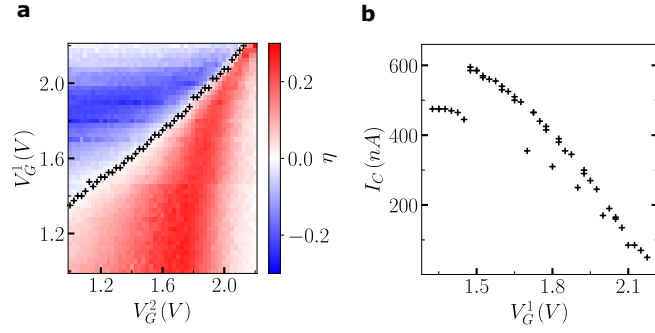


FIG. S8. **Balanced SQUID line.** **a**, Diode efficiency η at fixed applied flux $\Phi_{ext}/\Phi_0 = 0.45$ as a function of the two gate voltages V_G^1 and V_G^2 of the symmetric SQUID. The η minima are marked by the black crosses, they define to the sweet line. **b**, SQUID critical current I_C along the line as a function of the gate voltages V_G^1 while V_G^2 is adjusted to be in the zero diode efficiency regime.

S-VII. INFLUENCE OF THE DIODE EFFECT ON THE SHAPIRO PATTERNS

In Fig. S9, we study the Shapiro pattern in the unbalanced regime ($V_G^1 = 1.3$ V & $V_G^2 = 1.75$ V) for three different applied fluxes corresponding to a negative diode efficiency (Fig. S9b), a zero diode efficiency (Fig. S9c) and a positive diode efficiency (Fig. S9d). The bias current ramps always start from zero toward positive/negative values so that the forward/backward current configurations are probed. We note that the Shapiro steps width are also affected by the diode effect. The kink in the backward (resp. forward) I_C power dependency observed in Fig. S9b (resp. Fig. S9d) remains unexplained.

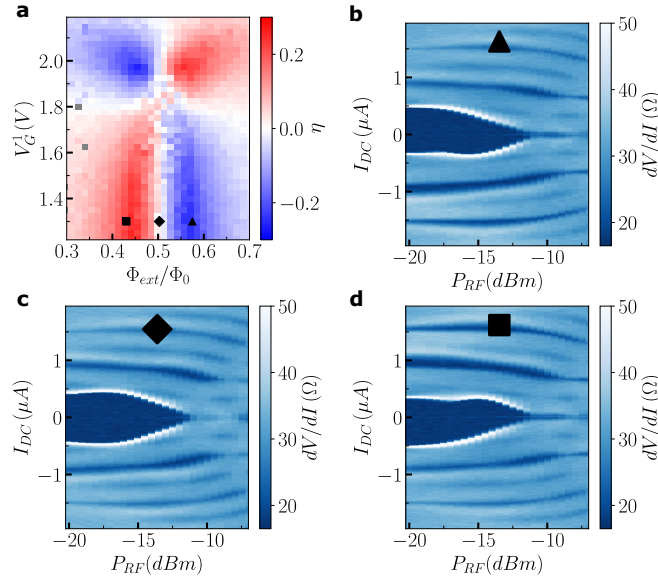


FIG. S9. **Shapiro patterns at negative, null and positive diode efficiency.** **a**, Zoom in the diode efficiency pattern shown in Fig. 4b where η is plotted as function of J_1 gate voltage (V_G^1) and the applied magnetic flux Φ_{ext} . V_G^2 is kept at 1.75 V. The three signs (\blacksquare , \blacklozenge , \blacktriangle) indicate the gate and flux configurations at which the Shapiro patterns are measured. **b,c,d**, Shapiro patterns measured by current biasing always from zero to positive/negative values at $V_G^1 = 1.3$ V and $V_G^2 = 1.75$ V. The flux biasing is kept at $\Phi_{ext}/\Phi_0 = 0.57$ in **b**, $\Phi_{ext}/\Phi_0 = 0.5$ in **c** and $\Phi_{ext}/\Phi_0 = 0.43$ in **d**.

S-VIII. ADDITIONAL SHAPIRO MEASUREMENTS AROUND THE SECOND HARMONIC ENHANCEMENT SWEET SPOT

During a new cool down of the same device, we focus on the center of the diode efficiency pattern shown in Fig. 4b and notice that it is not exactly symmetric. Thus, we investigate the Shapiro patterns in this region and find that

the presence or absence of integer Shapiro steps correlates mainly with the applied magnetic flux and not with the gate voltage fine tuning.

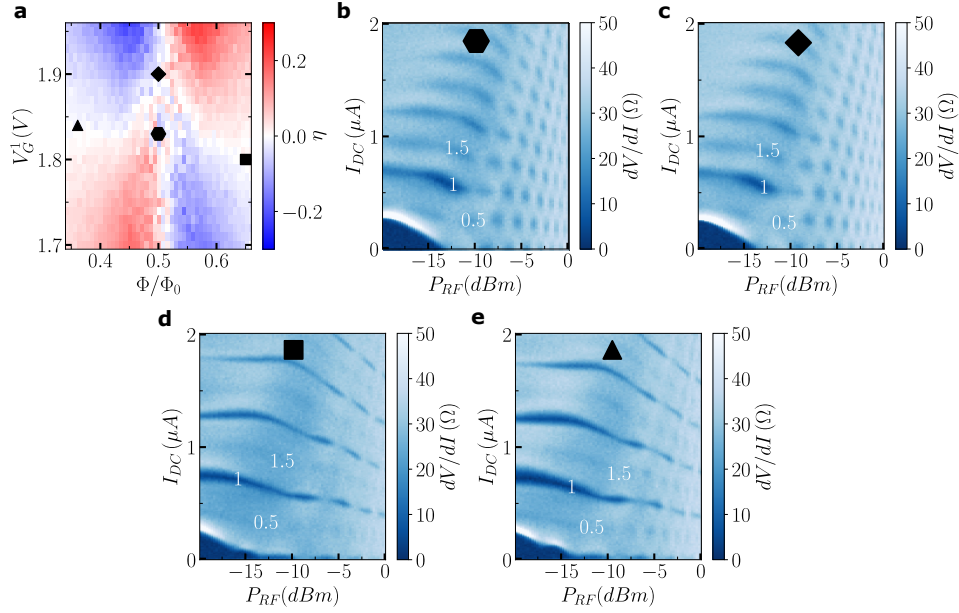


FIG. S10. **Shapiro patterns around the balanced SQUID and half flux sweet spot configuration.** **a**, Diode efficiency η as a function of the J_1 gate voltage V_G^1 and the applied magnetic flux Φ_{ext} . V_G^2 is kept at 1.75 V. The four signs indicate the gate and flux configurations at which the Shapiro patterns are measured. **b,c,d,e**, All the Shapiro patterns are measured at $V_G^2 = 1.75$ V. J_1 gate voltage and magnetic flux bias are $V_G^1 = 1.83$ V and $\Phi_{ext}/\Phi_0 = 0.5$ in **b**, $V_G^1 = 1.9$ V and $\Phi_{ext}/\Phi_0 = 0.5$ in **c**, $V_G^1 = 1.8$ V and $\Phi_{ext}/\Phi_0 = 0.65$ in **d**, $V_G^1 = 1.84$ V and $\Phi_{ext}/\Phi_0 = 0.36$ in **e**.

S-IX. SYMMETRIC SQUID CURRENT PHASE RELATION

We compute the current phase relation (CPR) of a symmetric SQUID. The two junction CPRs are modeled by the short junction single channel at zero temperature formula [14], which gives the current I as a function of the junction phase φ for a given transparency τ :

$$I(\varphi) = \frac{e\Delta}{2\hbar} \frac{\tau \sin(\varphi)}{\sqrt{1 - \tau \sin^2(\varphi/2)}} \quad (\text{S14})$$

where e is the elementary charge, \hbar the reduced Plank constant and Δ the superconducting gap. Thus, the total SQUID CPR is the sum of the two junction CPRs considering the fluxoid relation:

$$I_{SQUID}(\varphi) = I_1(\varphi) + I_2(\varphi - 2\pi\Phi/\Phi_0) \quad (\text{S15})$$

where I_1 (resp. I_2) is the CPR of the junction J_1 (resp. J_2), φ is the J_1 phase, Φ is the applied magnetic flux through the SQUID and $\Phi_0 = h/2e$ is the flux quantum. Fig. S11 shows the computed CPR and its harmonic decomposition for a SQUID where the junctions transparency are $\tau = 0.7$.

At integer flux quantum, the SQUID CPR contains odd and even harmonics but at half flux quantum, the odd harmonics vanish and so the fundamental frequency doubles. Furthermore, at quarter flux quantum, we notice that the even harmonics vanish. Considering only the first two harmonics (the amplitudes of the next ones are usually negligible), the SQUID behaves as a so-called $\sin(2\varphi)$ Josephson element at half the flux quantum, as a pure $\sin(\varphi)$ at quarter flux quantum and as a multi harmonics element at integer flux quantum.

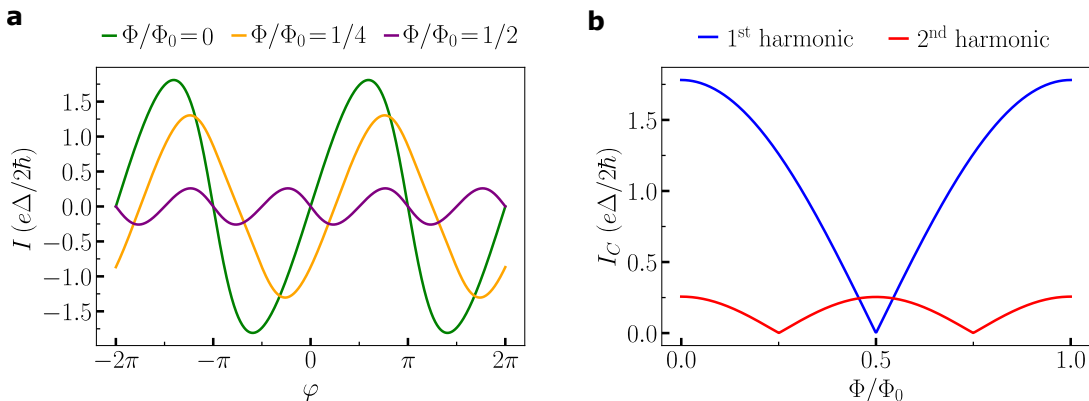


FIG. S11. **Computation of a symmetric SQUID CPR for a single channel short junction model with a transparency $\tau = 0.7$.** **a**, The SQUID CPR for different flux bias values. The normalized current I flowing through the SQUID is plotted as a function of the phase of one of the two junctions. **b**, The two first harmonic contributions to the SQUID critical current I_C of the same system plotted as a function of the normalized magnetic flux Φ/Φ_0 .